

Cite this: DOI: 00.0000/xxxxxxxxxx

Structural evolution of binary oxide nanolaminates with annealing and its impact on room-temperature internal friction

Le Yang,^{*a} Mariana Fazio,^b and Gabriele Vajente,^c Alena Ananyeva,^c GariLynn Billingsley,^d Ashot Markosyan,^d Riccardo Bassiri,^d Martin M. Fejer,^d Carmen S. Menoni^{b‡}

Received Date
Accepted Date

DOI: 00.0000/xxxxxxxxxx

Internal friction in oxide thin films imposes a critical limitation to the sensitivity and stability of ultra-high finesse optical cavities for gravitational wave detectors. Strategies like doping or creating nanolaminates are sought to introduce structural modifications that reduce internal friction. This work describes an investigation of the morphological changes $\text{SiO}_2/\text{Ta}_2\text{O}_5$ and $\text{TiO}_2/\text{Ta}_2\text{O}_5$ nanolaminates undergo with annealing and their impact on room temperature internal friction. It is demonstrated that thermal treatment results in a reduction of internal friction in both nanolaminates, but through different pathways. In the $\text{SiO}_2/\text{Ta}_2\text{O}_5$ nanolaminate, which layers remain intact after annealing, the total reduction in internal friction follows the reduction in the composing SiO_2 and Ta_2O_5 layers. Instead, interdiffusion initiated by annealing at the interface of the $\text{TiO}_2/\text{Ta}_2\text{O}_5$ nanolaminate and the formation of a mixed phase dictate a more significant reduction in internal friction to $\sim 2.6 \times 10^{-4}$, a value lower than any other Ta_2O_5 mixture coating with similar cation concentration.

1 Introduction

Nanolaminates are representative engineered materials that consist of stacks of nanometer-thick layers of two or more dissimilar materials. These two-dimensional composite thin films are extensively used in semiconductor devices^{1–3}, electrochemical storage devices⁴, and optical coatings^{5,6}. Their unique properties arise from modifications to the environment of atoms at nanometer to subnanometer scale. For example, in nanolaminates of $\text{Al}_2\text{O}_3/\text{ZnO}$ ⁷ an exponential increase in emission intensity was achieved due to quantum confinement when the ZnO sublayer thickness was reduced to less than 2 nm. The large interfacial area between layers also plays a critical role in modifying the structural properties of nanolaminates. In $\text{HfO}_2/\text{Al}_2\text{O}_3$ ⁸ and $\text{HfO}_2/\text{La}_2\text{O}_3$ ⁹ nanolaminates it is found that the amorphous state of HfO_2 can be stabilized up to 800 °C annealing, an effect created by the increased contribution from surface enthalpy to the total film energy. At the interface, when chemical reactions occur,

advantageous functional properties develop, as is the formation of robust Al-O-Ti and Al-O-Zr bonds that inhibit water incorporation in $\text{Al}_2\text{O}_3/\text{TiO}_2$ ^{10,11} and $\text{Al}_2\text{O}_3/\text{ZrO}_2$ nanolaminates¹². The improved water anticorrosion is ascribed to the formation of a ternary phase that is thermodynamically more stable than separate phases of the binary oxides^{13,14}.

The ability to alter structural properties in nanolaminates has also stimulated great interest for their use in highly reflective mirror coatings of ultrastable optical cavities. High finesse cavities are essential components for precision measurements of time and space, such as atomic clocks and gravitational wave detectors^{15,16}. For these applications, reducing thermally driven fluctuation is critical to stabilizing the cavity length and thus improving the system's sensitivity. For example, a factor of four reduction in internal friction (Q^{-1}) of the mirror coating in the vicinity of 100 Hz would expand the ability of the Advanced LIGO to detect astrophysical events beyond its present limit, 120 megaparsecs^{17–19}. Nanolaminates are envisioned to replace the high index layers in the current mirror coatings. The structural modifications associated with the nanolaminate architecture are expected to alter medium range order of the atomic structure and hence the sources of internal friction, which are conceptualized as two-level systems (TLSs)²⁰. Experiments on $\text{TiO}_2/\text{SiO}_2$ nanolaminates have shown pronounced suppression of internal friction at cryogenic temperatures²¹. This behavior was attributed to the interruption of long scale building blocks associated with TLSs

^a Department of Chemistry, Colorado State University, Fort Collins, CO 80523, USA; E-mail: yangle@colostate.edu

^b Department of Electrical and Computer Engineering, Colorado State University, Fort Collins, CO 80523, USA

^c LIGO Laboratory, California Institute of Technology, Pasadena, CA 91125, USA

^d Edward L. Ginzton Laboratory, Stanford University, Stanford, CA 94305, USA

† Electronic Supplementary Information (ESI) available. See DOI: 00.0000/00000000.

‡ Carmen.Menoni@colostate.edu

by constraining the layer thickness. In contrast, a direct observation and an unambiguous identification of the structural features that relate to the reduction in room temperature internal friction is still lacking. Identifying and understanding the key structural evolution that governs the internal friction behavior will accelerate the search for coating materials for the next generation gravitational wave detectors.

Herein, we describe the behavior of room temperature internal friction of $\text{SiO}_2/\text{Ta}_2\text{O}_5$ and $\text{TiO}_2/\text{Ta}_2\text{O}_5$ nanolaminates with the goal to identify the origin of internal friction reduction in these amorphous oxide thin films. It is shown that the morphological and structural evolution of the $\text{SiO}_2/\text{Ta}_2\text{O}_5$ nanolaminate upon annealing is significantly different from that of the $\text{TiO}_2/\text{Ta}_2\text{O}_5$ nanolaminate. The interfaces between layers remain sharp up to an annealing temperature of 650°C in the $\text{SiO}_2/\text{Ta}_2\text{O}_5$ nanolaminate. Instead, interdiffusion in the $\text{TiO}_2/\text{Ta}_2\text{O}_5$ nanolaminate is revealed by high resolution transmission electron microscopy. In both cases, annealing lowers internal friction compared to a single Ta_2O_5 layer, but from different origin. The reduction in internal friction of the $\text{SiO}_2/\text{Ta}_2\text{O}_5$ nanolaminate results from the combined reduction in the individual Ta_2O_5 and SiO_2 nanolayers. Instead, interdiffusion and formation of a stable ternary phase upon annealing is responsible for the reduction of internal friction in the $\text{TiO}_2/\text{Ta}_2\text{O}_5$ nanolaminate.

2 Experimental

Nanolaminates of $\text{SiO}_2/\text{Ta}_2\text{O}_5$ and $\text{TiO}_2/\text{Ta}_2\text{O}_5$ were prepared by reactive ion beam sputtering using a biased target deposition system²². A high purity metal target is sputtered by Ar ions when a negative bias of 800 V is applied to the target. Ultra-high purity oxygen gas is introduced to the chamber near the substrate surface to grow oxides. Optimization of the oxygen flow was carried out to ensure stoichiometry of the oxides. Deposition rates of Ta_2O_5 , TiO_2 and SiO_2 were measured to be 0.17, 0.022 and 0.058 \AA/s , respectively. The low deposition rates offer a high control in layer thickness and interfacial quality when depositing nanometer thick layers. The samples were designed to have a 6 nm top layer of Ta_2O_5 and 15 pairs of 1.6 nm SiO_2 or TiO_2 and 6 nm Ta_2O_5 (Figure 1). The stacks were deposited onto fused silica and silicon substrates by sequentially biasing the corresponding metal targets. For these designs, the cation concentration $\text{Si}/(\text{Si}+\text{Ta})$ and $\text{Ti}/(\text{Ti}+\text{Ta})$ is $\sim 20\%$. Reference mixture samples of the same cation concentration were also prepared. The mixture cation composition is controlled by varying the target bias time in one period.

The nanolaminate and mixture samples were annealed in air by ramping up the temperature at 1.6°C/min and soaking at the set temperature for 10 hrs with a Fisher Scientific Isotemp programmable furnace. Soaking temperatures were varied in steps of 100°C up to the highest temperature at which the first sign of crystallization appeared.

The structure evolution with annealing was characterized by grazing incidence x-ray diffraction (GIXRD) using a Bruker D8 thin film diffractometer operated at an incident angle of 0.5° . X-ray photoelectron spectroscopy (XPS) measurements were carried out with a PE-5800 to examine the bonding environments of the

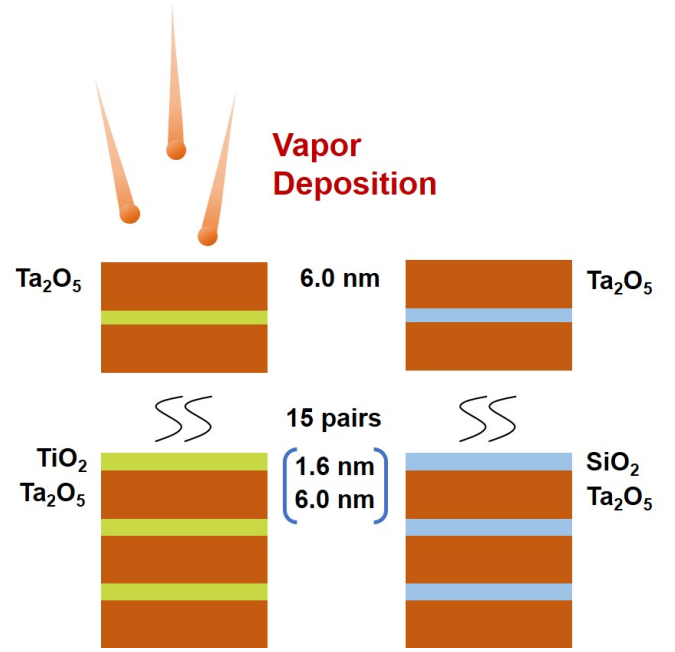


Fig. 1 Schematic of the nanolaminate samples with a 6 nm top layer of Ta_2O_5 and 15 pairs of 1.6 nm SiO_2 or TiO_2 and 6 nm Ta_2O_5 .

elements. A take-off angle of 45° was used for all scans. The neutralizer operating at $10 \mu\text{A}$ was used to counteract charging effect of the sample. The C 1s peak position was used to calibrate the binding energy scale of the spectra. The peak shapes were fitted with Gaussian functions. High resolution transmission electron microscopy images of as-deposited and annealed nanolaminates were obtained using a FEI Tecnai Osiris FEG/TEM operated at 200 kV by EAG Laboratories.

The evaluation of the internal friction for each sample was performed with a coating ring-down system^{23–25} by Vajente et al at the LIGO laboratory, Caltech. A gentle nodal suspension was used to support the sample within a vacuum chamber with a pressure below 10^{-6} Torr. After exciting the resonant mode, the decay of the oscillation amplitude was measured for each sample to obtain the internal friction.

3 Results and discussion

Figure 2 shows the room temperature internal friction of the $\text{SiO}_2/\text{Ta}_2\text{O}_5$ and $\text{TiO}_2/\text{Ta}_2\text{O}_5$ nanolaminates for different annealing temperatures. For as-deposited nanolaminates, $\text{TiO}_2/\text{Ta}_2\text{O}_5$ has a higher $Q^{-1} \approx (7.5 \pm 0.2) \times 10^{-4}$ than $\text{SiO}_2/\text{Ta}_2\text{O}_5$ with $Q^{-1} \approx (6.9 \pm 0.5) \times 10^{-4}$. This is due to as-deposited SiO_2 single layer having low Q^{-1} ²⁶. Upon increasing the annealing temperature from 400°C to 500°C , the trend is reversed in that Q^{-1} of the $\text{TiO}_2/\text{Ta}_2\text{O}_5$ is lower than that of the $\text{SiO}_2/\text{Ta}_2\text{O}_5$ nanolaminate. At 650°C , the internal friction of the $\text{TiO}_2/\text{Ta}_2\text{O}_5$ nanolaminate reaches its lowest value of $Q^{-1} \approx (2.6 \pm 0.2) \times 10^{-4}$. At this temperature, Q^{-1} is $(3.1 \pm 0.2) \times 10^{-4}$ for the $\text{SiO}_2/\text{Ta}_2\text{O}_5$ nanolaminate. In both cases, these values are lower than the best value for a single layer Ta_2O_5 annealed at 500°C , $Q^{-1} \approx 4.0 \times 10^{-4}$ ²⁷. For comparison, the inset of Figure 2 plots internal friction of the nanolaminates and mixtures of $\text{SiO}_2/\text{Ta}_2\text{O}_5$ and

TiO₂/Ta₂O₅ at the highest annealing temperature before crystallization. For the SiO₂/Ta₂O₅ nanolaminate, Q^{-1} is lower than that of the reference mixture of $Q^{-1} \approx 4.1 \times 10^{-4}$ after 700°C annealing. Phase separation after annealing in the SiO₂/Ta₂O₅ mixture results in a Q^{-1} value similar to that of a single layer Ta₂O₅ (Figure S1). Instead, Q^{-1} is the same within experimental errors for the TiO₂/Ta₂O₅ nanolaminate and mixture after annealing, indicating a strong similarity. In both the mixture and nanolaminate form, the TiO₂/Ta₂O₅ system exhibits lower internal friction than that of the SiO₂/Ta₂O₅ one.

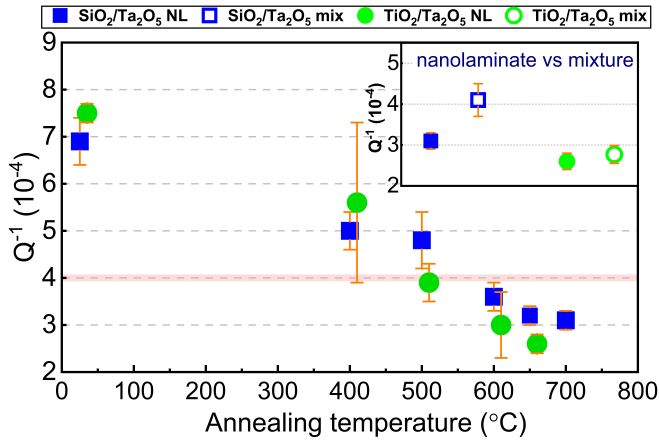


Fig. 2 Room temperature internal friction of nanolaminates as-deposited and annealed at different temperatures. The SiO₂/Ta₂O₅ nanolaminate (NL) is represented by blue filled squares and the TiO₂/Ta₂O₅ nanolaminate (NL) is represented by green filled circles. After annealing at 500°C, the TiO₂/Ta₂O₅ nanolaminate has a lower internal friction than the SiO₂/Ta₂O₅ nanolaminate. Inset, internal friction of the SiO₂/Ta₂O₅ nanolaminate annealed at 700°C, the SiO₂/Ta₂O₅ mixture annealed at 700°C (blue open square), the TiO₂/Ta₂O₅ nanolaminate annealed at 650°C, and the TiO₂/Ta₂O₅ mixture annealed at 600°C (green open circle). The red shading indicates the internal friction level of a single layer Ta₂O₅ annealed at 500°C.

There are significant differences in the structural evolution upon annealing that affect the internal friction behavior of the nanolaminates. The high resolution TEM images of the as-deposited TiO₂/Ta₂O₅ and SiO₂/Ta₂O₅ nanolaminates show well defined layers with sharp interfaces (Figure 3). Upon annealing at 650°C, the SiO₂/Ta₂O₅ nanolaminate remains unchanged, showing intact interfaces between strongly contrasted SiO₂ and Ta₂O₅ layers. In this case, the Q^{-1} can be approximated as the weighted average of the internal friction of the composing oxide layers (disregarding any interfacial effects)^{21,28}. This calculation estimates $Q^{-1} \approx 3.4 \times 10^{-4}$, which is in good agreement with the measured value. On the contrary, a noticeable discontinuity along the interfaces and a homogenization of the two oxide materials are found in the annealed TiO₂/Ta₂O₅ nanolaminate.

Full crystallization of the TiO₂/Ta₂O₅ and SiO₂/Ta₂O₅ nanolaminates is observed after annealing at 750°C and 800°C, respectively. The crystallization process is delayed to a higher annealing temperature in both nanolaminates compared to 675°C, the crystallization temperature of a single layer Ta₂O₅²⁷, due to a greater contribution from the surface enthalpy to the total energy^{9,29,30}. Diffraction patterns of the crystallized nanolaminates

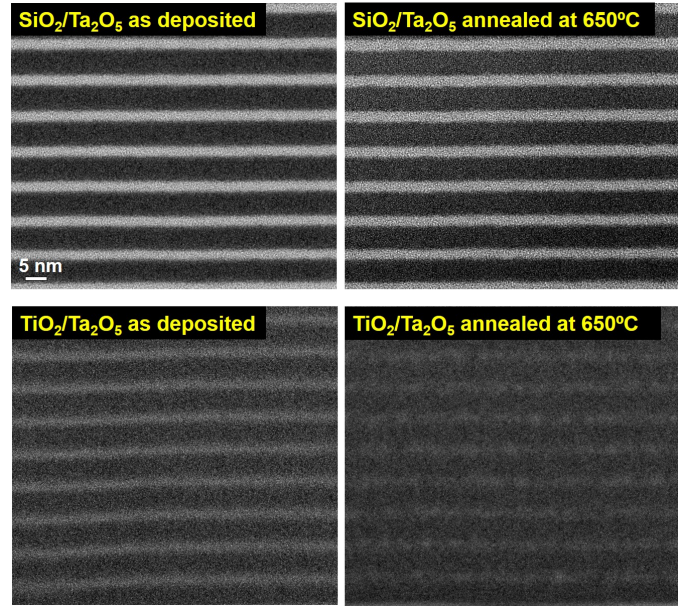


Fig. 3 High resolution cross-sectional TEM images of nanolaminates before and after annealing at 650°C. Top, SiO₂/Ta₂O₅ nanolaminate showing robust layer structure before and after annealing. Bottom, TiO₂/Ta₂O₅ nanolaminate showing interface blurring after annealing.

and the crystallized Ta₂O₅ single layer are shown in Figure 4. The spectrum of the crystallized SiO₂/Ta₂O₅ nanolaminate only exhibits diffraction peaks from the orthorhombic Ta₂O₅ phase³¹ while no SiO₂ peak is found. The peaks feature a much broader profile than that of a single layer Ta₂O₅. Applying the Scherrer equation³² to the peak at $2\theta = 28.7^\circ$, the crystallite size in the SiO₂/Ta₂O₅ nanolaminate is calculated to be ~ 5 nm, while a size of 35 nm is calculated for the single layer Ta₂O₅. The crystallite size of 5 nm is fully consistent with the Ta₂O₅ layer thickness ~ 6 nm, indicating the physical constraint to crystallite growth imposed by the interfaces. The same analysis of the TiO₂/Ta₂O₅ nanolaminate yields a crystallite size of 11 nm that is larger than the layer thickness. The extended growth is only possible when bi-directional diffusion across the interface bridges the separated Ta₂O₅ layers.

The emergence of Ti 2p peaks in the XPS spectrum confirms a strong Ti cation diffusion into the top Ta₂O₅ layer in the TiO₂/Ta₂O₅ nanolaminate upon annealing (Figure S2). Instead, a Si 2p peak is almost absent in the XPS spectrum of both as-deposited and annealed SiO₂/Ta₂O₅ nanolaminates. Figure 5 shows the Ti 2p core level in the TiO₂/Ta₂O₅ nanolaminate after annealing at 650°C. The peak separation is determined to be $\sim 5.85 \pm 0.02$ eV, which is significantly different from 5.7 eV for Ti in a TiO₂(IV) environment³³. The change in peak separation is ascribed to the Ta-O-Ti bonding process that accompanies the mixing of TiO₂ and Ta₂O₅. The mixing in this sample is the same as observed in a TiO₂/Ta₂O₅ mixture upon annealing, which leads to the formation of a ternary compound identified as TiTa₁₈O₄₇ that is thermodynamically more stable than separate phases of TiO₂ and Ta₂O₅³⁴. The existence of a stable ternary phase in nanolaminates has been well demonstrated in systems

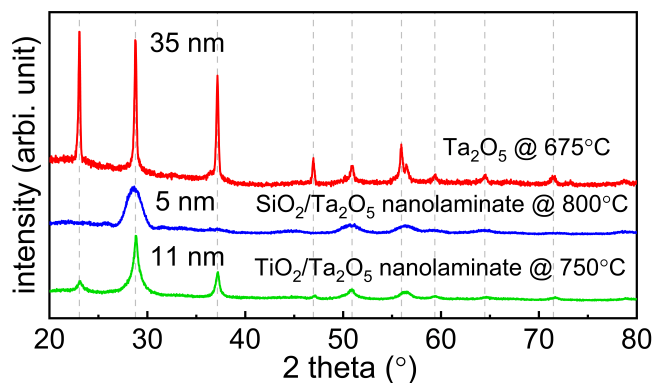


Fig. 4 Diffraction patterns of the $\text{SiO}_2/\text{Ta}_2\text{O}_5$ nanolaminate annealed at 800°C (blue line) and the $\text{TiO}_2/\text{Ta}_2\text{O}_5$ nanolaminate annealed at 750°C (green line) after crystallization. For comparison, the diffraction spectrum of a crystallized Ta_2O_5 single layer annealed at 675°C is shown on top (red line).

such as $\text{Al}_2\text{O}_3/\text{TiO}_2$ ^{10,11} and $\text{Al}_2\text{O}_3/\text{ZrO}_2$ ^{12,14}, where the presence of the mixed phase gives superior physical and/or chemical properties that can be used in various applications. In the absence of a stable ternary phase, a cross-interface diffusion between layers should not occur as it will not lead to a reduction in Gibbs free energy for the whole system. Such picture is supported by the observation of well spaced layers in the $\text{SiO}_2/\text{Ta}_2\text{O}_5$ (Figure 3) and $\text{SiO}_2/\text{TiO}_2$ ²¹ nanolaminates after annealing.

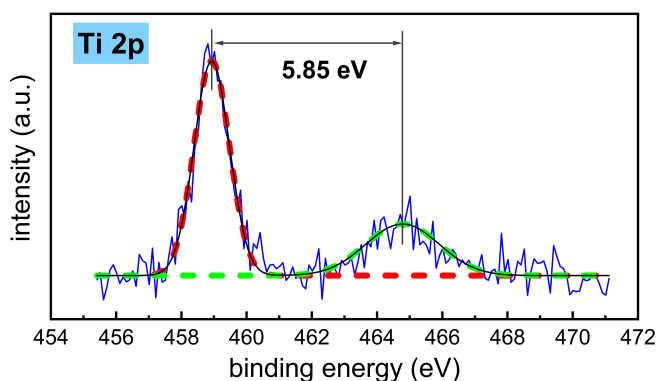


Fig. 5 X-ray photoelectron spectrum of Ti 2p in the $\text{TiO}_2/\text{Ta}_2\text{O}_5$ nanolaminate after annealing at 650°C . The peak separation is determined to be 5.85 eV. Collected spectrum after background subtraction is shown in blue line, the composite spectrum is shown in black line, the Ti 2p $3/2$ peak is shown in red dashed line, and the Ti 2p $1/2$ peak is shown in green dashed line.

These results show that in these binary oxide nanolaminates, the more significant reduction in room temperature internal friction is dominated by interdiffusion and the formation of a stable mixed phase rather than the effect of nanolayering of the two oxide materials. For the $\text{TiO}_2/\text{Ta}_2\text{O}_5$ nanolaminate, it is the reorganization that occurs during the mixing that has a major influence on reducing the room temperature internal friction. Elevated annealing temperature in the $\text{SiO}_2/\text{Ta}_2\text{O}_5$ nanolaminate improves the internal friction with respect to a single layer Ta_2O_5 due to a reduction of internal friction in both the SiO_2 and Ta_2O_5 nanolayers. The internal friction of an annealed SiO_2 layer reaches Q^{-1}

$\approx 0.5 \times 10^{-4}$ that is the lowest value among all binary oxide films²⁶. Yet the reduction is not as profound as from mixing in the $\text{TiO}_2/\text{Ta}_2\text{O}_5$ nanolaminate. This behavior is different from what has been observed for the cryogenic internal friction of $\text{SiO}_2/\text{TiO}_2$ nanolaminates, which manifests itself by a decrease in internal friction with a decrease in layer thickness²¹. Such effect is ascribed to the elimination of two-level system transitions with characteristic dimensions that exceed the layer thickness. At room temperature, however, contribution from those cryogenic two-level systems to the internal friction is negligibly small³⁵ so that the effect from nanolayering does not lead to lower internal friction. On the contrary, observation of the structural evolution in the $\text{TiO}_2/\text{Ta}_2\text{O}_5$ nanolaminate with annealing suggests that the formation of a more stable phase might result in the modified distribution of two-level systems that is responsible for lowering the room temperature internal friction.

4 Conclusions

An unambiguous identification of the morphological changes that involve layer breakup and mixture formation in the $\text{TiO}_2/\text{Ta}_2\text{O}_5$ nanolaminate is demonstrated. The mixing of TiO_2 and Ta_2O_5 , which is thermodynamically favored upon annealing, results in the major improvements in the room temperature internal friction of the $\text{TiO}_2/\text{Ta}_2\text{O}_5$ nanolaminate. In the absence of mixing, the reduction in room temperature internal friction of a nanolaminate with annealing can be predicted from the changes in the composing layers, as is the case of the $\text{SiO}_2/\text{Ta}_2\text{O}_5$ nanolaminate. A modified distribution of two-level systems in the mixed phase rather than size effects is argued to be responsible for the more profoundly reduced room temperature internal friction in the $\text{TiO}_2/\text{Ta}_2\text{O}_5$ nanolaminate. These results are significant in that they provide new insight into the suppression of two-level systems and pave the way towards a more delineated search of new coating materials with low internal friction that potentially will increase the sensitivity of the next generation gravitational wave detectors.

Conflicts of interest

There are no conflicts to declare.

Acknowledgements

This work is supported by the National Science Foundation LIGO program through grants No. 1710957 and 1708010. We also acknowledge the support of the LSC Center for Coatings Research, jointly funded by the National Science Foundation (NSF) and the Gordon and Betty Moore Foundation. A. M., R. B. and M. M. F. are grateful for support through NSF awards PHY-1707866, PHY-1708175 and GBMF Grant No. 6793. Partial support from grant ONR No. N00014-17-1-2536 is acknowledged. We thank Riccardo DeSalvo, Innocenzo Pinto, and Manel Molina Ruiz for useful discussions.

Notes and references

- 1 P. Tsipas, S. Volkos, A. Sotiropoulos, S. Galata, G. Mavrou, D. Tsoutsou, Y. Panayiotatos, A. Dimoulas, C. Marchiori and J. Fompeyrine, *Applied physics letters*, 2008, **93**, 082904.

- 2 G. Wilk, R. Wallace and J. Anthony, *Journal of Applied Physics*, 2000, **87**, 484–492.
- 3 F. Boscherini, F. D'Acapito, S. Galata, D. Tsoutsou and A. Dimoulas, *Applied Physics Letters*, 2011, **99**, 121909.
- 4 X. Huo, X. Wang, Z. Li, J. Liu and J. Li, *Nanoscale*, 2020, **12**, 3387–3399.
- 5 N. K. Sahoo and A. P. Shapiro, *Applied optics*, 1998, **37**, 8043–8056.
- 6 L. Karvonen, A. Säynätjoki, Y. Chen, H. Jussila, J. Rönn, M. Ruoho, T. Alasaarela, S. Kujala, R. A. Norwood, N. Peyghambarian *et al.*, *Applied Physics Letters*, 2013, **103**, 031903.
- 7 J. Li and X. Bi, *Nanoscale*, 2017, **9**, 16420–16428.
- 8 T. Wang and J. G. Ekerdt, *Chemistry of Materials*, 2011, **23**, 1679–1685.
- 9 T. Wang and J. G. Ekerdt, *Chemistry of Materials*, 2009, **21**, 3096–3101.
- 10 L. H. Kim, K. Kim, S. Park, Y. J. Jeong, H. Kim, D. S. Chung, S. H. Kim and C. E. Park, *ACS Applied Materials & Interfaces*, 2014, **6**, 6731–6738.
- 11 L. H. Kim, Y. J. Jeong, T. K. An, S. Park, J. H. Jang, S. Nam, J. Jang, S. H. Kim and C. E. Park, *Physical Chemistry Chemical Physics*, 2016, **18**, 1042–1049.
- 12 J. Meyer, P. Görrn, F. Bertram, S. Hamwi, T. Winkler, H.-H. Johannes, T. Weimann, P. Hinze, T. Riedl and W. Kowalsky, *Advanced materials*, 2009, **21**, 1845–1849.
- 13 C. Zhao, O. Richard, H. Bender, M. Caymax, S. De Gendt, M. Heyns, E. Young, G. Roebben, O. Van der Biest and S. Haukka, *Applied physics letters*, 2002, **80**, 2374–2376.
- 14 J. Meyer, H. Schmidt, W. Kowalsky, T. Riedl and A. Kahn, *Applied Physics Letters*, 2010, **96**, 117.
- 15 G. D. Cole, W. Zhang, M. J. Martin, J. Ye and M. Aspelmeyer, *Nature Photonics*, 2013, **7**, 644–650.
- 16 N. Morell, A. Reserbat-Plantey, I. Tsioutsios, K. G. Schädler, F. Dubin, F. H. Koppens and A. Bachtold, *Nano letters*, 2016, **16**, 5102–5108.
- 17 J. Miller, L. Barsotti, S. Vitale, P. Fritschel, M. Evans and D. Sigg, *Physical Review D*, 2015, **91**, 062005.
- 18 G. Vajente, E. K. Gustafson and D. H. Reitze, *Advances In Atomic, Molecular, and Optical Physics*, Elsevier, 2019, vol. 68, pp. 75–148.
- 19 B. P. Abbott, R. Abbott, T. Abbott, M. Abernathy, F. Acernese, K. Ackley, C. Adams, T. Adams, P. Addesso, R. Adhikari *et al.*, *Living Reviews in Relativity*, 2018, **21**, 3.
- 20 C. R. Billman, J. P. Trinstic, D. J. Davis, R. Hamdan and H.-P. Cheng, *Physical Review B*, 2017, **95**, 014109.
- 21 L.-C. Kuo, H.-W. Pan, C.-L. Chang and S. Chao, *Optics letters*, 2019, **44**, 247–250.
- 22 K. G. West, J. Lu, J. Yu, D. Kirkwood, W. Chen, Y. Pei, J. Claassen and S. A. Wolf, *Journal of Vacuum Science & Technology A: Vacuum, Surfaces, and Films*, 2008, **26**, 133–139.
- 23 G. Vajente, A. Ananyeva, G. Billingsley, E. Gustafson, A. Heptonstall, E. Sanchez and C. Torrie, *Review of Scientific Instruments*, 2017, **88**, 073901.
- 24 E. Cesarini, M. Lorenzini, E. Campagna, F. Martelli, F. Piergiovanni, F. Vetrano, G. Losurdo and G. Cagnoli, *Review of Scientific Instruments*, 2009, **80**, 053904.
- 25 M. Granata, A. Amato, G. Cagnoli, M. Coulon, J. Degallaix, D. Forest, L. Mereni, C. Michel, L. Pinard, B. Sassolas *et al.*, *Applied Optics*, 2020, **59**, A229–A235.
- 26 R. Flaminio, J. Franc, C. Michel, N. Morgado, L. Pinard and B. Sassolas, *Classical and Quantum Gravity*, 2010, **27**, 084030.
- 27 L. Yang, E. Randel, G. Vajente, A. Ananyeva, E. Gustafson, A. Markosyan, R. Bassiri, M. M. Fejer and C. S. Menoni, *Physical Review D*, 2019, **100**, 122004.
- 28 M. Granata, E. Coillet, V. Martinez, V. Dolique, A. Amato, M. Canepa, J. Margueritat, C. Martinet, A. Mermet, C. Michel *et al.*, *Physical Review Materials*, 2018, **2**, 053607.
- 29 H.-W. Pan, S.-J. Wang, L.-C. Kuo, S. Chao, M. Principe, I. M. Pinto and R. DeSalvo, *Optics express*, 2014, **22**, 29847–29854.
- 30 L. Zhang, J. Zhang, H. Jiao, G. Bao, Z. Wang and X. Cheng, *Thin Solid Films*, 2017, **642**, 359–363.
- 31 C. Chanceliere, S. Four, J. Autran, R. Devine and N. Sandler, *Journal of applied physics*, 1998, **83**, 4823–4829.
- 32 J. I. Langford and A. Wilson, *Journal of applied crystallography*, 1978, **11**, 102–113.
- 33 D. Barreca, A. Gasparotto, C. Maccato, C. Maragno and E. Tondello, *Surface Science Spectra*, 2007, **14**, 27–33.
- 34 M. Fazio, G. Vajente, A. Ananyeva, A. Markosyan, R. Bassiri, M. Fejer and C. S. Menoni, *Opt. Mater. Express*, 2020, **10**, 1687.
- 35 J. Jiang, A. Mishkin, K. Prasai, M. Yazback, R. Zhang, R. Bassiri, M. Fejer and H. Cheng, <https://dcc.ligo.org/LIGO-P1900371>.